



Trans. Nonferrous Met. Soc. China 35(2025) 3240-3255

Transactions of Nonferrous Metals Society of China

www.tnmsc.cn



Simultaneously enhancing strength, ductility, and stiffness of lightweight multicomponent Mg-Al-Zn-Cu-Ce alloys

Zuo-hong GU^1 , Yun-xuan $ZHOU^{1,2,3}$, Jia-xing $PENG^1$, Guang-ming HE^1 , Hao LV^1 , Quan $DONG^1$, Jun $TAN^{1,2,3}$, Xian-hua $CHEN^{1,2,3}$, Bin $JIANG^{1,3}$, Fu-sheng $PAN^{1,2,3}$, Jürgen $ECKERT^{4,5}$

- 1. National Engineering Research Center for Magnesium Alloys, College of Materials Science and Engineering, Chongqing University, Chongqing 400044, China;
 - 2. Lanxi Magnesium Materials Research Institute, Lanxi 321100, China;
- 3. National Key Laboratory of Advanced Casting Technologies, Chongqing University, Chongqing 400044, China;
- 4. Erich Schmid Institute of Materials Science, Austrian Academy of Sciences, Jahnstraße 12, A-8700, Leoben, Austria;
 - 5. Department of Materials Physics, Montanuniversität Leoben, Jahnstraße 12, A-8700, Leoben, Austria

Received 16 January 2024; accepted 29 October 2024

Abstract: To obtain lightweight multicomponent magnesium alloys with high tensile strength, ductility, and stiffness, two extruded $Mg_{92-5x}Al_{1.5+3x}Zn_3Cu_{3.5+x}Ce_x$ (x=0.5 and 1, labeled as C0.5 and C1) alloys were designed. The results reveal that the ultimate tensile strength, yield strength (YS), and fracture strain of the C0.5 alloy are simultaneously improved compared to those of the C1 alloy, with values of 346 MPa, 312 MPa, and 11.7%, respectively. This enhancement is primarily attributed to the refinement of numerous secondary phases (micron scale Al₃CuCe, micron scale MgZnCu, and nanoscale MgZnCu phases). The calculation of YS shows that the Orowan strengthening and coefficient of thermal expansion mismatch strengthening are the main strengthening mechanisms, and the contribution values of both to the YS are 28 and 70 MPa for C0.5 alloy. In addition, the C0.5 alloy has a greater plasticity than the C1 alloy because the $\langle c+a \rangle$ slip system is initiated.

Key words: Mg-Al-Zn-Cu-Ce alloy; Al₃CuCe phase; strengthening mechanism; plastic deformation mechanism; mechanical properties

1 Introduction

Magnesium (Mg) alloys, which have excellent properties such as light weight [1,2], high specific strength [3], good conductivity, high damping capacity [4], and superior recyclability, have an excellent potential for application in automobile [5,6],aerospace [7,8],and 3C (computer, communication, and consumer electronics) industries [9,10]. Under the background of a low-carbon human lifestyle, developing Mg alloys with the lightweight and high mechanical properties is important. However, low strength, low stiffness, and poor plastic deformation of Mg alloys greatly hinder their large-scale applications [11]. The low Young modulus (*E*) of pure Mg is approximately 44 GPa, which dramatically impedes its engineering applications. The lightweight Mg-based multicomponent alloys (MCAs) are a unique class of alloys whose design concept is that one dominant principal element, Mg, is alloyed with several other constituent elements with significant atomic proportions [12]. The secondary phases (SPs) play a

crucial role in strengthening alloys owing to their high strength and stiffness, which leads to the Orowan strengthening ($\Delta\sigma_{\text{Orowan}}$), the coefficient of thermal expansion (CTE) mismatch strengthening ($\Delta\sigma_{\text{CTE}}$), the modulus mismatch strengthening ($\Delta\sigma_{\text{Modulus}}$), and the load transfer effect. Fine-sized particles and high volume fractions of SPs enhance the mechanical properties of alloys because of the increase in the particle/matrix interfacial boundary [13]. In contrast to traditional Mg alloys, MCAs contain alloying elements far exceeding those in traditional Mg alloys, resulting in the presence of numerous hard SPs within matrix. Consequently, MCAs exhibit significant yield strength (YS), compressive strength, hardness, and modulus.

It is an effective strategy to refine the particle size of SPs to reach the significant strengthening of alloys. Small SPs can effectively inhibit recrystallization and pin grain boundaries, thus enhancing the strength of alloy [14,15]. WU et al [16] investigated the effect of SP particles on grain growth in AZ31 Mg alloys using phase field simulations. They found that when the particle size exceeds a critical value of 1 µm, the pining effect on grain growth increases as the particle content decreases. However, when the particle size falls below this critical value, the trend reverses. In addition to refining the particle size of SPs, increasing their volume fraction can significantly strengthen the alloys. On the one hand, the particle/matrix interfacial boundary has a function of hindering the slide of dislocations; on the other hand, the misfit strain is generated by the mismatch in CTE between the reinforcement and matrix, which leads to the formation of the punch prismatic dislocation loops under thermal stress. ROSALIE et al [17] investigated the effect of precipitation on strength and ductility in Mg-Zn-Y alloy. They found that the increase in precipitate volume fraction and refining the precipitation microstructure substantially raised the yield strength (YS) from 217 to 287 MPa, which is related to the decrease of particle spacing as expected for Orowan looping of non-shearing particles. LI and LAVENDER [18] studied the strengthening and improving yield asymmetry of Mg alloys through the refinement of SP particle and the adjustment of their volume fraction. The results indicated that the grain size decreases with the increasing precipitate volume fraction and decreasing precipitate size. Moreover, the YS and compressive yield strength/tensile yield strength (CYS/TYS) increase with decreasing grain size and contributions from increasing precipitate volume fraction or decreasing precipitate size.

The lightweight MCAs usually contain a lot of SPs, and reach high mechanical properties, including good strength and hardness [19-21]. However, a fatal disadvantage is that the large size of SPs results in a bad applied performance in ductility. Our previous study demonstrated that increasing the volume fraction of stable intermetallic phases with high cohesive energy and E has achieved high strength and E of Mg alloys; however, the plasticity was very poor. Additionally, it was found that the Al₃CuCe phase exhibits high structural stability and is most accessible to grow with increasing Ce content in Mg-Al-Zn-Cu-Ce alloys. Thus, controlling the size of SPs can potentially obtain both excellent plasticity and strength in MCAs [12]. Moreover, the increase of the Al₃CuCe phase content is influenced not only by changes in Ce content, but also by variations in the amounts of Al and Cu elements. Therefore, the synchronized adjustments of Al, Cu, and Ce in the current study will influence the formation of the Al₃CuCe phase. Based on the above analysis, two new lightweight Mg-Al-Zn-Cu-Ce MCAs with high tensile strength, high E, and acceptable ductility are fabricated and followed by hot extrusion in this work. Hot extrusion is used to refine grain and SP size, and combine the advantages of abundance of SPs in MCAs, which makes it possible to achieve a breakthrough in tensile strength and E with acceptable ductility.

2 Experimental

2.1 Sample preparation

The previous studies have found that the Al₃CuCe phase exhibits high structural stability and is most accessible to grow with the increasing Ce content in Mg-Al-Zn-Cu-Ce alloys [12]. To control the particle size of SPs, the studied Mg₈₇Al_{4.5}Zn₃Cu_{4.5}Ce₁ (named as C1 alloy) and Mg_{89.5}Al₃Zn₃Cu₄Ce_{0.5} (named as C0.5 alloy) alloys, containing different amounts of Al₃CuCe phase, were fabricated using an electric resistance furnace under the protection of a mixed gas of CO₂ and SF₆ in a volume ratio of 99:1. The raw materials

including pure Mg (99.97 wt.%), Zn (99.9 wt.%), Al (99.7 wt.%), Cu (99.99 wt.%), and Mg⁻30wt.%Ce master alloy and stainless-steel crucibles (*d*89 mm × 280 mm) were used in this work. Rapid cooling was achieved by immersing the crucible into water to get grain refinement. The ingots with a diameter of 82 mm and a height of 50 mm were obtained, and underwent solution treatment at 400 °C for 24 h, followed by extrusion using a 500T–XJ horizontal extrusion machine at 350 °C with an extrusion ratio of 26:1. The actual compositions of the Mg–Al–Zn–Cu–Ce alloys, measured by an X-ray fluorescence spectrometer (XRF–1800), are listed in Table 1.

Table 1 Actual compositions of Mg-Al-Zn-Cu-Ce alloys measured by X-ray fluorescence spectrometer (at.%)

Alloy	Al	Zn	Cu	Се	Mg
C1	4.5	3.1	4.4	0.9	Bal.
C0.5	2.5	2.5	3.5	0.7	Bal.

2.2 Characterization and test methods

Phase identification was performed using an X-ray diffractometer (XRD, PANalytical Empyrean) with Cu K_{α} . Microstructural observations were carried out using scanning electron microscope (SEM, JEOL JSM7800F) equipped with an energy

dispersive spectrometer (EDS), electron back-scattered diffraction (EBSD, with a step size of 0.4 μm), and a transmission electron microscope (TEM, Talos F200S). Moreover, the polished specimens for SEM observations were etched by 4% nitric acid alcohol. The TEM specimens were first ground to approximately 50 μm in thickness followed by milling using a LEICA EM RES 102. Tensile tests at a strain rate of 0.0007 s⁻¹ were conducted using a CMT6305–300 KN electronic universal testing machine at room temperature.

3 Results

3.1 Mechanical behaviors

Figure 1 shows the mechanical properties of the as-extruded Mg–Al–Zn–Cu–Ce alloys. Figure 1(a) demonstrates the typical engineering stress–strain curves of the C1 and C0.5 alloys at a strain rate of $0.0007 \, \text{s}^{-1}$ at room temperature, using standard tensile samples size of $d5 \, \text{mm} \times 25 \, \text{mm}$. The results indicate that the C0.5 alloy achieves simultaneous improvements in both strength and ductility compared to the C1 alloy. Figure 1(b) presents the ultimate tensile strength (UTS), YS, and fracture strain (ε_f) of the C1 and C0.5 alloys. There is a substantial increase in UTS, YS, and ε_f of the C0.5 alloy compared to the C1 alloy. The UTS and YS of the C0.5 alloy increase from 319 and

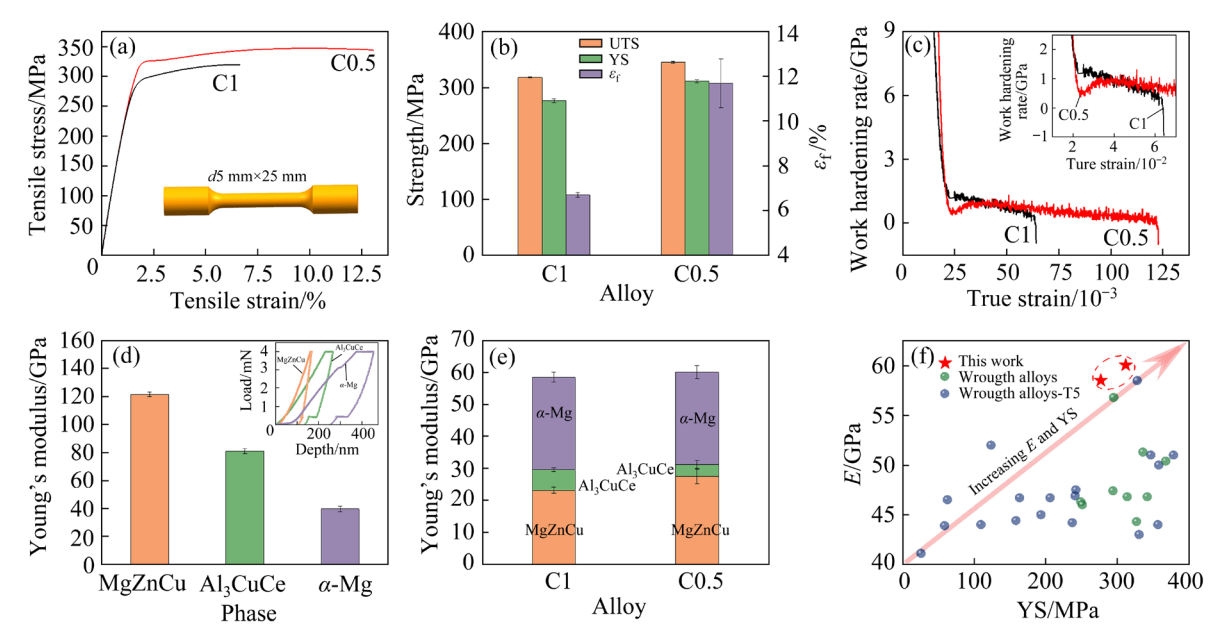


Fig. 1 Typical engineering stress-strain curves (a); Ultimate tensile strength, yield strength, and fracture strain (b), and work hardening rate (c) of C1 and C0.5 alloys; Young modulus of each phase with nanoindentation test result inserted (d); Contribution of each phase to Young modulus (e); Yield strength and Young modulus distribution of magnesium alloys reported in Refs. [22–30] (f)

277 MPa to 346 and 312 MPa, respectively, compared to the C1 alloy. In addition, the ε_f of the C0.5 alloy is almost twice that of the C1 alloy, increasing from 6.7% to 11.7%. Table 2 summarizes the mechanical properties and densities of the as-extruded Mg–Al–Zn–Cu–Ce alloys. The work hardening rate of the C1 alloy decreases during the tensile process, while C0.5 alloy exhibits a brief increase after yielding, as shown in Fig. 1(c).

Table 2 Summary of mechanical properties and densities of as-extruded Mg-Al-Zn-Cu-Ce alloys

A 11 av.	LITC/MDa	VC/MDa	o /0/	Density/
Alloy	UTS/MPa	YS/MPa	$\varepsilon_{\rm f}$ /%	$(g \cdot cm^{-3})$
C1	319.0±1.0	277.0±3.0	6.7 ± 0.1	2.19
C0.5	346.3±1.7	312.0±2.9	11.7±1.1	2.17

Figures 1(d, e) illustrate the E of the phases and their contributions in Mg-Al-Zn-Cu-Ce alloys. The nanoindentation tests reveal the E of MgZnCu, Al₃CuCe, and α -Mg phases, as shown in Fig. 1(d). The relationship between the E and the indentation depth (h) is given as follows [31]:

$$E = \frac{\sqrt{\pi}}{2\sqrt{S}} \frac{\mathrm{d}P}{\mathrm{d}h} \tag{1}$$

where S represents the projected contact surface area between the indenter and the matrix after the nanoindentation test. For the Berkovich triangular pyramid indenter, $S = 24.56h_c^2$, and h_c denotes the vertical depth of the contact surface. dP/dhrepresents the slope of the highest point of the unloading curve. The MgZnCu phase, serving as the main reinforcement phase, exhibits the highest E of 121.60 GPa. It is reasonable to conclude that the MgZnCu phase has significantly enhanced the E of the Mg-Al-Zu-Cu-Ce alloys. The E values of the Al₃CuCe and α-Mg phases reach 80.98 GPa (82.2 GPa calculated in our previous work [12]) and 39.70 GPa (45 GPa reported in another reference [32]), respectively. According to the rule of mixtures, the contribution of each phase to the Ecan be estimated, as illustrated in Fig. 1(e). The E of the C1 alloy is calculated to be 58.53 GPa, with contributions from the MgZnCu, Al₃CuCe, and α -Mg being 23.13, 6.45, and 28.95 GPa, respectively. For the C0.5 alloy, the contribution to E from the MgZnCu phase increases to 27.53 GPa, while the contribution from the Al₃CuCe phase

decreases to 3.61 GPa. The E of the C0.5 alloy increases to 60.08 GPa compared to that of the C1 alloy, which is achieved by increasing the volume fraction of the high modulus MgZnCu phase. Figure 1(f) shows a comparison of YS and E for some typical Mg alloys, including a few commercial alloys [22-25], and high rare earth alloys [22,26–30]. Thus, the current work demonstrates high YS and elastic modulus compared to other reported Mg alloys in the literature, as listed in Table 3. It can be seen from Table 3 and Fig. 1(f) that the YS and UTS in this work are slightly lower than certain rare earthcontaining Mg alloys, but the E in this work exhibits an outstanding advantage. Moreover, the C0.5 and C1 alloys contain fewer rare earth elements, thus providing a cost-effective advantage. In addition, the densities of the C0.5 and C1 alloys were measured using the Archimedes method, which are 2.17 and 2.19 g/cm³, respectively. The C0.5 alloy has exceptionally high YS, excellent elastic modulus, and low density, coupled with low cost, making it particularly suitable for engineering applications.

3.2 Microstructures

Figures 2 and 3 present the microstructure, XRD patterns, and volume fraction of each SPs in the as-extruded Mg-Al-Zn-Cu-Ce alloys. There are two different color contrasts in the matrix. The brighter one shows a large size block-like (Fig. 2(a)) or rod-like morphology (Fig. 2(b)), while the other one has the morphology of fine-sized particles. Combined with the results from the XRD patterns (Fig. 3(a)), which indicate that the main identified phases are α -Mg, Al₃CuCe, and MgZnCu, it can be concluded that the bright phase is Al₃CuCe, while the other phase is MgZnCu. Figures 2(c, d) show the high magnification images of the C1 and C0.5 alloys, respectively. In comparison to the C1 alloy, the C0.5 alloy has finer size Al₃CuCe and MgZnCu phases. In addition, the corresponding EDS point scan data in Figs. 2(c, d) are presented in Table 4. Notably, Point A in Fig. 2(c) and Point H in Fig. 2(d) correspond to the Mg matrix. The Points B, C, and D in Fig. 2(c) and Points I, J, and K in Fig. 2(d) are Al₃CuCe phases, and the Points E, F, and G in Fig. 2(c) and Points L, M, and N in Fig. 2(d) are MgZnCu phases. The nanoparticles are observed in matrix, but they are challenging to identify in SEM

Table 3 Corresponding data of mechanical properties and Young modulus in literature

Alloy	State	UTS/MPa	TYS/MPa	EL/%	E/GPa
Mg [22]	As-extruded	115	25	6.0	41.1
	As-rolled (RD)		158		44.4
Mg-3Al-1Zn [23]	As-rolled (ND)		62		46.5
	As-rolled (45°)		58		43.9
Mg-3Al-1Zn [24]	As-extruded	271	237	4.4	44.2
Mg-3Al-1Zn [25]	As-extruded	213	193	9.7	45.0
Mg-12Gd-1Zn-0.5Zr-0.5Ag [22]	As-extruded	171	109	5.4	44.0
Mg-12Gd-1Zn-0.5Zr-0.5Ag-6Al-5Li [22]	As-extruded	199	123	22.5	52.0
Mg-10Gd-1.5Ag-0.2Mn [26]	As-extruded	374	331	10.4	43.0
Mg-10Gd-1.5Ag-0.2Mn-1.5Ge [26]	As-extruded	414	358	10.2	50.0
Mg-10Gd-1.5Ag-0.2Mn-3.5Ge [26]	As-extruded	423	379	10.0	51.0
M 1001 2N11271	As-extruded	339	163	20.6	46.7
Mg-10Gd-2Nd [27]	As-extruded-T5	406	249	9.0	46.3
M 1001 5N11971	As-extruded	357	206	14.3	46.7
Mg-10Gd-5Nd [27]	As-extruded-T5	365	251	6.0	46.0
M 1501 2011[27]	As-extruded	403	241	15.6	46.9
Mg-15Gd-2Nd [27]	As-extruded-T5	401	314	4.9	46.8
M 1501 5N11971	As-extruded	356	242	11.1	47.5
Mg-15Gd-5Nd [27]	As-extruded-T5	365	294	4.4	47.4
Mg-8.0Gd-4.0Y-1.0Nd-1.0Zr [28]	As-extruded	423	357	3.4	44.0
Mg-8.0Gd-4.0Y-1.0Nd-1.0Zr-1.0Si [28]	As-extruded	392	347	2.7	51.0
Mg-12Gd-3Y-0.5Zn-0.6Zr [29]	As-rolled-T5	411	327	3.6	44.3
Mg-12Gd-3Y-0.5Zn-0.6Zr-0.5Sn [29]	As-rolled-T5	428	342	4.3	46.8
Mg-12Gd-3Y-0.5Zn-0.6Zr-1Sn [29]	As-rolled-T5	452	368	5.7	50.4
Mg-12Gd-3Y-0.5Zn-0.6Zr-2Sn [29]	As-rolled-T5	422	336	5.2	51.3

images. Figure 3(b) demonstrates the volume fraction of the Al₃CuCe and MgZnCu phases. The C0.5 alloy exhibits a finer particle size for the MgZnCu phase and fewer large-sized Al₃CuCe phases, which mainly cause the enhancement of ductility of the C0.5 alloy compared to the C1 alloy.

To further investigate the precipitation of nanoparticle phases in the matrix, TEM was employed to analyze the microstructure of the C0.5 alloy. Figure 4 shows the TEM images along with energy-dispersive X-ray (EDX) analysis and selected area electron diffraction (SAED) patterns. The Point 1, characterized by an EDX result showing similar atomic fractions of Mg, Zn and Cu, is identified as the MgZnCu phase with the SAED pattern oriented along [110] direction. It has a

cubic structure with the lattice constants of a=b=c=0.7154 nm. The rod-like phase marked as Point 2 is identified as the Al₃CuCe phase with [010] direction in the SAED pattern. It has a tetragonal structure with the lattice constants of a=b=0.4261 nm and c=1.0652 nm. The nanoparticle phase has a cubic structure with the lattice constants of a=b=c=0.7170 nm, corresponding to the nano-MgZnCu structure.

4 Discussion

4.1 Strengthening mechanisms

4.1.1 Grain size

It is essential to reveal the grain size to discuss the mechanical properties, corresponding to the

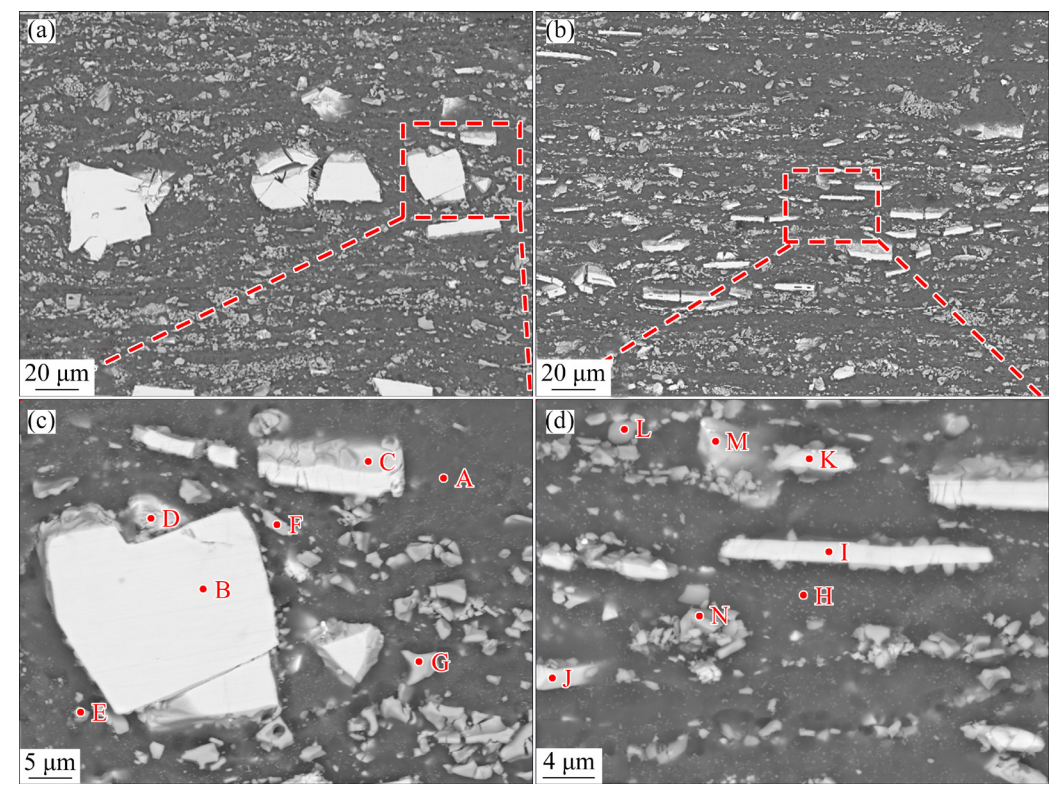


Fig. 2 Microstructures of as-extruded Mg-Al-Zn-Cu-Ce alloys: (a, c) C1 alloy; (b, d) C0.5 alloy

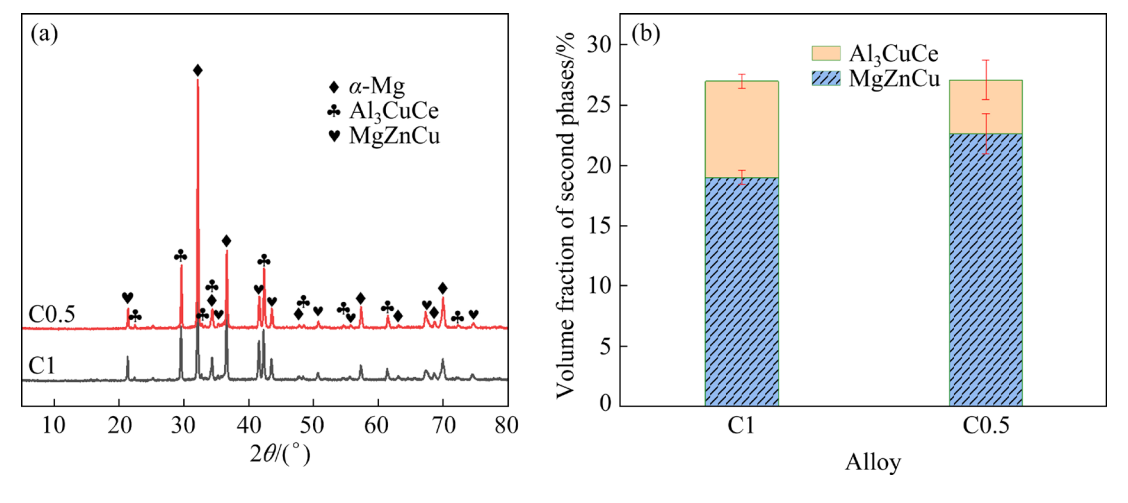


Fig. 3 XRD patterns (a) and volume fraction of secondary phase (b) in as-extruded Mg-Al-Zn-Cu-Ce alloys

Hall–Petch effect. Band contrast (BC) images of the Mg–Al–Zn–Cu–Ce alloys, along with their grain size distribution, are shown in Figs. 5 and 6. Additionally, the vertical direction is parallel to the extrusion direction in Fig. 5. The average grain size of the C1 alloy is $\sim 10.1 \, \mu m$ (Fig. 6(a)). In contrast, the grain size of the C0.5 alloy is slightly smaller than that of the C1 alloy, measuring $\sim 8.7 \, \mu m$ (Fig. 6(b)). The smaller grain size typically correlates with higher strength and better fracture strain of the alloys. Additionally, the large size of

the SPs (Figs. 2(a, b)) during the hot deformation process can enhance particle-induced nucleation, resulting in a finer grain size of the C0.5 alloy. Simultaneously, grains near the SPs are finer than those far away from the SPs, indicating that the SPs can promote dynamic recrystallization during the extrusion process.

4.1.2 Secondary phase size

The Orowan strengthening mechanism indicates that reducing particle size enhances the alloy's strength by impeding the movement of

Table 4 Corresponding EDS point scan data in Figs. 2(c, d)

A 11 - D : 4		Content/at.%				
Alloy	Point	Mg	Al	Zn	Cu	Се
	A	99.0		0.6	0.4	
	В	4.0	52.4	3.2	19.9	20.6
	C	9.4	49.0	8.2	20.6	12.8
C1	D	13.0	34.5	9.0	28.7	14.8
	E	58.0	3.2	10.5	27.9	0.5
	F	41.8	2.1	25.0	30.7	0.4
	G	52.7	4.3	17.0	25.7	0.3
C0.5	Н	97.8		0.7	0.9	0.6
	I	7.6	49.7	4.9	21.4	16.3
	J	13.2	44.9	4.8	18.4	18.8
	K	7.5	46.9	7.3	22.8	15.6
	L	76.9		11.5	5.8	5.8
	M	28.8	19.4	14.3	29.6	7.8
	N	41.7	3.9	25.8	28.3	0.3

dislocation. Figure 7 presents size statistics of the Al₃CuCe and MgZnCu phases in the C1 and C0.5 alloys. The Al₃CuCe phase has two size statistics along the radial direction (RD) and the extrusion direction (ED) for its rod-like shape. The average size of the Al₃CuCe phase in the C0.5 alloy is significantly smaller than that in the C1 alloy, both along ED and RD. Additionally, d_{90} is 5.09 µm for the Al₃CuCe particles along the RD in the C0.5 alloy, while in the C1 alloy, it is 19.33 µm along the RD. In the ED direction, d_{90} is 20.62 µm for the Al₃CuCe particles in the C0.5 alloy, whereas it is 35.61 µm in the C1 alloy. Additionally, the MgZnCu particle size exhibits a similar trend to that of the Al₃CuCe phase. In the C0.5 alloy, d_{90} is 2.67 µm for the MgZnCu particles, much finer than those in the C1 alloy. Smaller particle sizes lead to more effective Orowan strengthening, resulting in higher mechanical strength of the alloys.

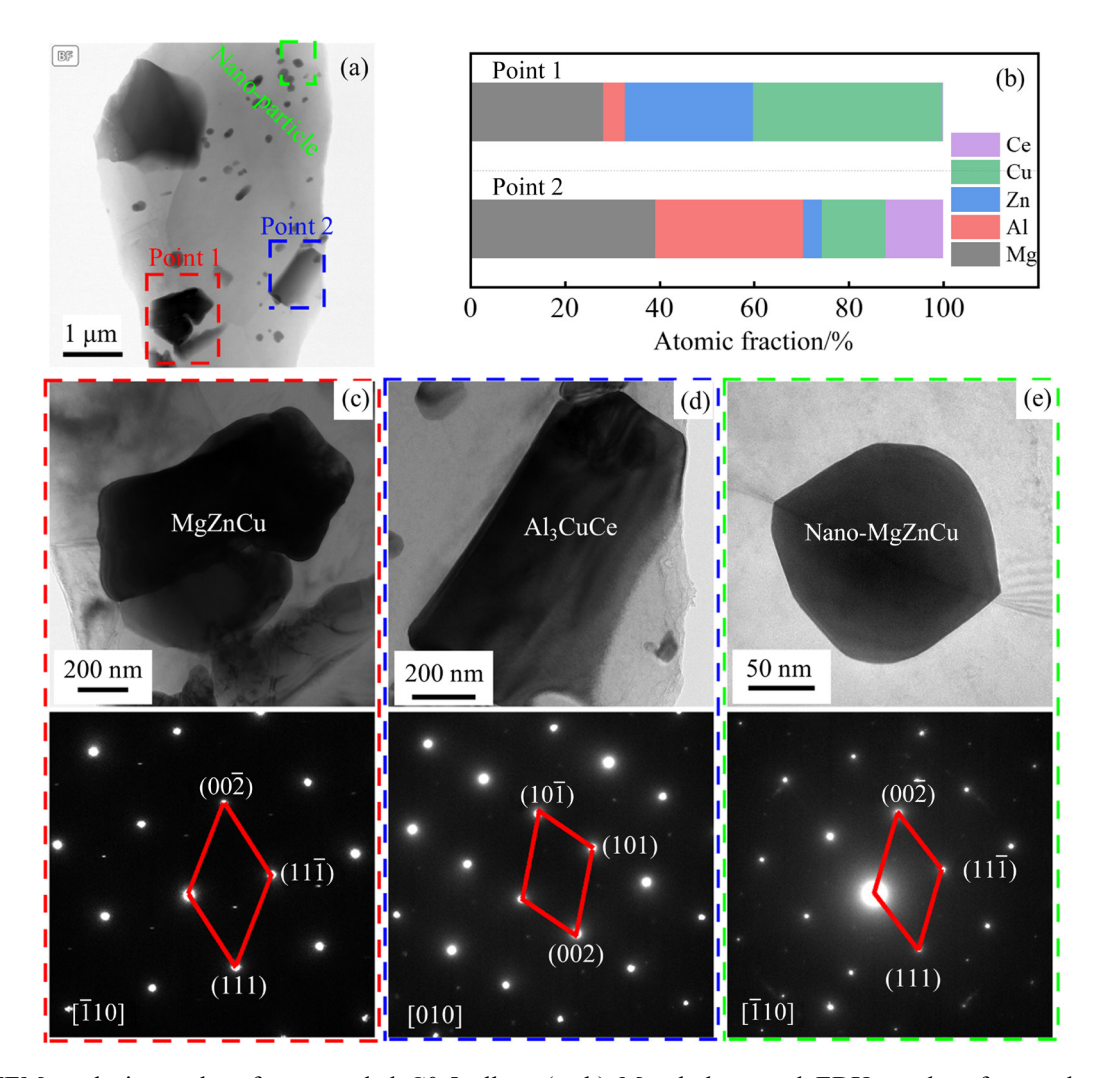


Fig. 4 TEM analysis results of as-extruded C0.5 alloy: (a, b) Morphology and EDX results of secondary phases; (c, d, e) TEM images and SAED patterns of MgZnCu, Al₃CuCe, and nano-MgZnCu phases, respectively

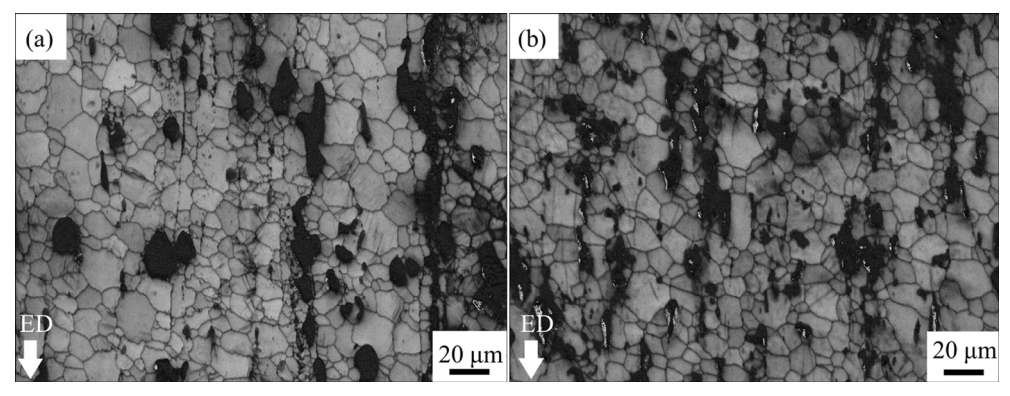


Fig. 5 Band contrast images of as-extruded Mg-Al-Zn-Cu-Ce alloys: (a) C1 alloy; (b) C0.5 alloy

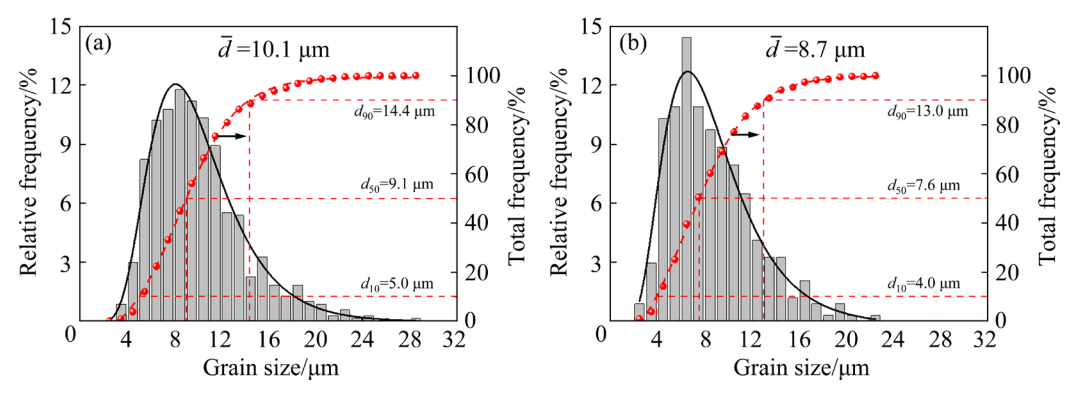


Fig. 6 Grain size distribution of as-extruded Mg-Al-Zn-Cu-Ce alloys: (a) C1 alloy; (b) C0.5 alloy

Some nano-MgZnCu phases precipitate in the matrix (Figs. 2(c, d)), and the particle size and distribution of the nano-MgZnCu phase are shown in Figs. 7(g, h). In the C1 alloy, the average particle size of the nano-MgZnCu is 205.58 nm, and d_{90} =402.64 nm. In the C0.5 alloy, the average particle size reaches 136.54 nm, which is significantly smaller than that of the C1 alloy. According to the Zener–Smith pining equation, the nanoparticle phase can significantly enhance the strength of alloys compared to the coarser one [33], contributing to the improved performance of the C0.5 alloy.

4.1.3 Calculation of yield strength

The strengthening mechanisms in this study are associated with the Hall–Petch effect ($\Delta\sigma_{\text{H-P}}$), the Orowan strengthening ($\Delta\sigma_{\text{Orowan}}$), the CTE mismatch strengthening ($\Delta\sigma_{\text{CTE}}$), the modulus mismatch strengthening ($\Delta\sigma_{\text{Modulus}}$), and the load transfer effect ($\Delta\sigma_{\text{Load}}$). The quadratic summation method is usually used to predict the YS of the alloys, as illustrated below [34]:

$$\sigma_{y} = \sigma_{0} + \frac{k}{d^{1/2}} + \left(\Delta \sigma_{\text{Orowan}}^{2} + \Delta \sigma_{\text{CTE}}^{2} + \Delta \sigma_{\text{Modulus}}^{2} + \Delta \sigma_{\text{Load}}^{2}\right)^{1/2}$$
(2)

where σ_0 is the friction stress when the dislocations slide on the slip plane, k is the stress concentration factor, and d is the grain size of the Mg matrix. In this study, σ_0 and k are equal to 130 MPa and 182 MPa· μ m^{1/2} [35], respectively. Grain boundary can pile up the dislocation during deformation, and the stress concentration is formed in this area, which needs a larger applied stress to generate the dislocations in the adjacent grains to continue the deformation of the alloys [36,37].

Secondary phase particles hinder the movement of dislocations, leaving either a dislocation loop around them or a cutting plane on the particles, thereby enhancing the strength of materials. A higher number of particles and smaller particle sizes contribute to increased strength, and thus, it is important to consider the Orowan strengthening in this study. $\Delta \sigma_{\text{Orowan}}$ can be roughly described by the Orowan–Ashby equation [38]:

$$\Delta \sigma_{\text{Orowan}} = \frac{0.13 G_{\text{m}} b}{d_{\text{p}} [(2V_{\text{p}})^{-1/3} - 1]} \ln \left(\frac{d_{\text{p}}}{2b} \right)$$
 (3)

where $G_{\rm m}$ and b are the shear modulus and the magnitude of Burgers vector of the Mg matrix, respectively; $d_{\rm p}$ and $V_{\rm p}$ are the size and volume

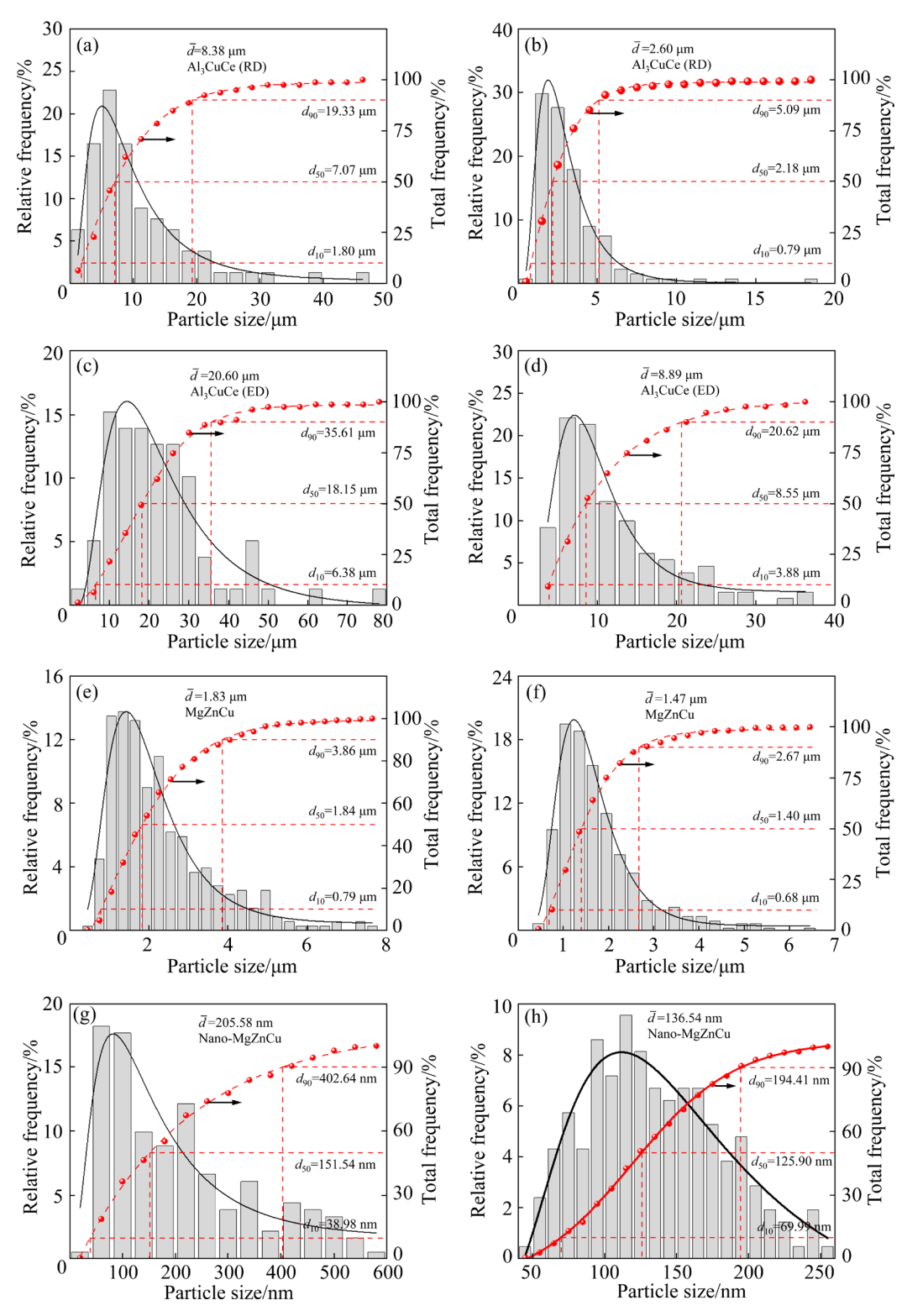


Fig. 7 Particle size and distribution of Al₃CuCe phases along radial direction (RD) (a, b) and extrusion direction (ED) (c, d), MgZnCu phases (e, f), as well as nano-MgZnCu phases (g, h) in Cl (a, c, e, g) and C0.5 (b, d, f, h) alloys

fraction of the reinforcement, respectively. The Mg matrix has a shear modulus ($G_{\rm m}$) of approximately 16.9 GPa and a magnitude of Burgers vector (b) of 0.32 nm [39].

When the alloys are cooled from extrusion

temperature to room temperature, misfit strains are generated due to the difference in the CTE between the reinforcement and the Mg matrix, resulting in punch prismatic dislocation loops caused by thermal stresses. The CTE mismatch strengthening,

hence, occurs in the alloys. The CTE mismatch strengthening can be described by the following formula [40]:

$$\Delta \sigma_{\rm CTE} = MAG_{\rm m}b\sqrt{\rho_{\rm CTE}} \tag{4}$$

where M is the Taylor factor (~5 in C1 and C0.5 alloys), which is assumed to be equal to the inverse of the Schmid factor. A is the strain-hardening constant with a value of 0.5 (between 0.3 and 0.6 for metals [41]). ρ_{CTE} is the dislocation density in the matrix due to punching, which can be calculated by the following formula [42]:

$$\rho_{\text{CTE}} = \frac{BV_{\text{p}}\varepsilon_{\text{m}}}{b(1 - V_{\text{p}})} \frac{1}{t}$$
 (5)

where B is a geometric constant (12 for equiaxed MgZnCu particles and 10 for rod-liked Al₃CuCe particles), and t is the smallest dimension of the particle. $\varepsilon_{\rm m}$ is the misfit strain as a result of the difference of thermal coefficient (Δ CTE) between the matrix and the particle, as shown in the following equation [42]:

$$\varepsilon_{\rm m} = \Delta {\rm CTE} \cdot \Delta T$$
 (6)

where ΔT is the difference between the extrusion temperature and room temperature, which is equal to 325 K in this work. Moreover, first-principles calculations employing density functional theory (DFT) were conducted utilizing the Vienna Ab-initio Simulation Package code (VASP), and projector augmented wave (PAW) method. The exchange-correlation functional of generalized gradient approximation (GGA) by Perdew-Burke-Ernzerhof (PBE) was utilized. A plane-wave energy cutoff of 380 eV was set, and for the Brillouin zone, the k-mesh sizes were $10\times10\times6$, $10\times10\times4$, and 8×8×8 for Mg, Al₃CuCe, and MgZnCu phases, respectively. The electronic self-consistent iteration convergence threshold was set to be 1.0×10^{-8} eV, and the force acting on each atom was less than 0.001 eV/Å. Moreover, the values of CTE were calculated and implemented in VASP in conjunction with the Phonopy code [43,44], which were found to be $24.83 \times 10^{-6} \,\mathrm{K}^{-1}$ (approximately $26 \times 10^{-6} \,\mathrm{K}^{-1}$ reported in Ref. [45]), $23.87 \times 10^{-6} \,\mathrm{K}^{-1}$, and $15.8 \times$ 10⁻⁶ K⁻¹ for Mg matrix, MgZnCu, and Al₃CuCe phases, respectively.

In addition to aforementioned strengthening mechanisms, the modulus mismatch strengthening mechanism can also contribute to enhancing the strength of alloys. It describes the generation of geometrically necessary dislocations when an alloy is subjected to tensile loading. The modulus mismatch strengthening can be calculated using the following relationship [46]:

$$\Delta \sigma_{\text{Modulus}} = 3\alpha G_{\text{m}} \sqrt{2V_{\text{p}}\varepsilon b/d_{\text{p}}}$$
 (7)

where α is a material-specific coefficient, which is 0.5 for mixed dislocations [47]. ε is the yield strain of the alloys, which is 0.2%.

The transfer of the load from the Mg matrix to the hard reinforcement is considered when an external load is applied. This contribution is proportional to both the size and volume fraction of the reinforcement. In the present study, due to the very high volume fraction of the reinforcement and the large range of particle sizes, the contribution of the load transfer effect to the strengthening is considered. It can be described by the following equation [48]:

$$\Delta \sigma_{\text{Load}} = \frac{(L+l)}{4l} \sigma_{\text{m}} V_{\text{p}}$$
 (8)

where L and l are the lengths of particles parallel and perpendicular to the loading direction, and $\sigma_{\rm m}$ is the YS of the Mg matrix with a value of 252 MPa [49].

The calculated contribution of strengthening mechanisms to the YS of C1 and C0.5 alloys is shown in Fig. 8, and the red lines represent the $\Delta \sigma$ curves changing with the particle sizes in this work, and the red points are the calculated $\Delta \sigma$ values in this work. Figure 8(a) shows the calculated $\Delta \sigma_{\text{CTE}}$ curves of MgZnCu phases with varying volume fractions and particle sizes. It can be seen that $\Delta \sigma_{\rm CTE}$ increases with an increasing volume fraction and decreasing particle sizes of the MgZnCu phases. The smaller the particle size is, the higher the amplification of the $\Delta \sigma_{\rm CTE}$ is. Because the nano-size MgZnCu phase in the C0.5 alloy has a smaller particle size and higher volume fraction than that in the C1 alloy, the calculated $\Delta \sigma_{\text{CTE}}$ of the C0.5 alloy is almost twice as high as that of the C1 alloy. For the micro-size MgZnCu phase, the calculated $\Delta \sigma_{\rm CTE}$ of the C0.5 alloy is also higher than that of the C1 alloy. The ΔCTE between Al₃CuCe and Mg matrix is much higher than the value between MgZnCu and Mg matrix. Thus, the Al₃CuCe has a higher $\Delta \sigma_{\rm CTE}$ than the MgZnCu at the same particle size and volume fraction, as indicated by the dotted line in Fig. 8(b). The calculated $\Delta \sigma_{\rm CTE}$ of the C0.5 alloy

is much higher than the value of the C1 alloy. Figure 8(c) shows the curves based on the Orowan strengthening mechanism with different volume fractions and particle sizes of the SPs. The size effect for the Orowan strengthening mechanism is more evident. It is hard to improve the strength of alloys by increasing the volume fraction of the SPs when the particle size reaches micron level. At the nano-size, the MgZnCu phase provides the main strength enhancement, and the value of the C0.5 alloy is almost twice as much as that of C1 alloy. The contribution of the Al₃CuCe phase is too small to consider because of their large particle size. Figure 8(d) shows the results of each strengthening mechanism and the calculated and experimental YS values. Table 5 gives the summary of the calculated

results of each strengthening mechanism. As observed, the highest part is from the Hall-Petch effect, but the value difference between the C1 and C0.5 alloys is small, which is not the main reason for the enhanced strength of the alloy. The second high part is the $\Delta \sigma_{\rm CTE}$, and the value of the C0.5 alloy is much higher than that of the C1 alloy, which is considered the most important strengthening mechanism in this work. The $\Delta\sigma_{\text{Orowan}}$ and $\Delta \sigma_{\text{Modulus}}$ of the C0.5 alloy are also higher than the values of the C1 alloy. It is worth noting that calculated σ_y is very close to experimental value, which means that the calculated value is credible. However, the calculated σ_0 is smaller than the experiment value, which might be attributed to other enhancement factors.

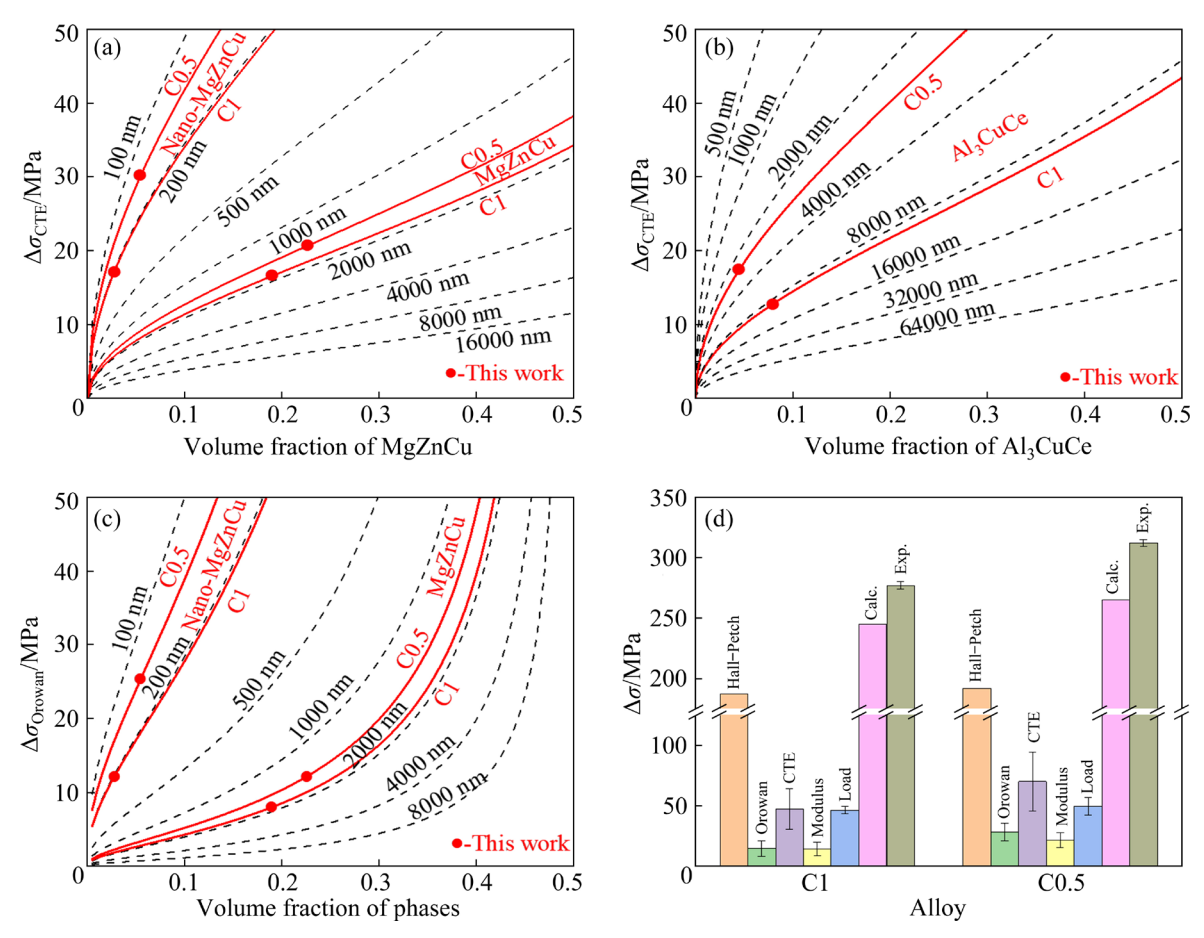


Fig. 8 Calculated $\Delta\sigma_{CTE}$ (a, b) and $\Delta\sigma_{Orowan}$ (c) curves of Mg-Al-Zn-Cu-Ce alloys with different volume fractions and particle sizes of MgZnCu (a) and Al₃CuCe (b) phases; Results of each strengthening mechanism and calculated and experiment values of yield strength (d)

Table 5 Summary of calculated results of each strengthening mechanism (MPa)

Alloy	$\Delta\sigma_{ m Orowan}$	$\Delta\sigma_{ m CTE}$	$\Delta\sigma_{ m Modulus}$	$\Delta\sigma_{ m Load}$	$\Delta\sigma_{ ext{H-P}}$	$\Delta\sigma_{ m Calc.}$
C1	14.65±6.41	27.41±9.71	14.21±5.63	46.52±2.87	187.27	244.99
C0.5	28.13±7.28	40.52 ± 14.08	21.52±6.10	49.66±7.19	191.73	264.96

4.2 Plastic deformation mechanisms

4.2.1 Texture and dynamic recrystallization

The EBSD test was used to analyze grain structure, grain orientation, and texture of the alloy. Figure 9 illustrates the grain orientation and pole figures of the C1 and C0.5 alloys. The texture intensity of the alloy is generally not high due to the presence of numerous SPs, which promote the dynamic recrystallization. The peak intensity of the C0.5 alloy is 5.63, which is weaker than that of the C1 alloy (7.89).

Grain orientation spread (GOS) is an effective technique for identifying the recrystallized microstructure in deformed or partially recrystallized samples [50]. It is generally believed that when the GOS of the grain is greater than 1°, the grain is considered to be deformed or unrecrystallized, while it is considered to be a recrystallized grain when the GOS is less than 1°. Figure 10 shows the distribution of GOS. The recrystallization degree of C1 and C0.5 alloys is high, which is attributed to the large number of SPs that promote the dynamic recrystallization.

4.2.2 In-grain misorientation axe analysis

Table 6 lists the main slip systems in Mg alloys and their corresponding Taylor axes [23].

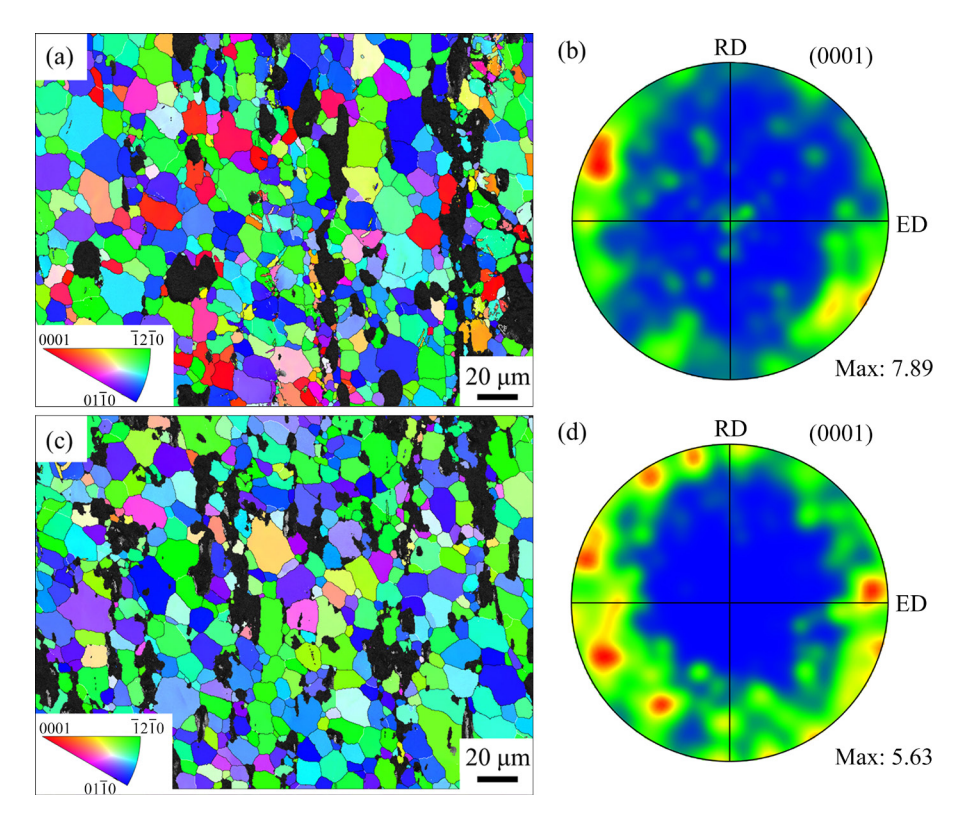


Fig. 9 Grain orientation (a, c) and pole figures (b, d) of Mg-Al-Zn-Cu-Ce alloys: (a, b) C1 alloy; (c, d) C0.5 alloy

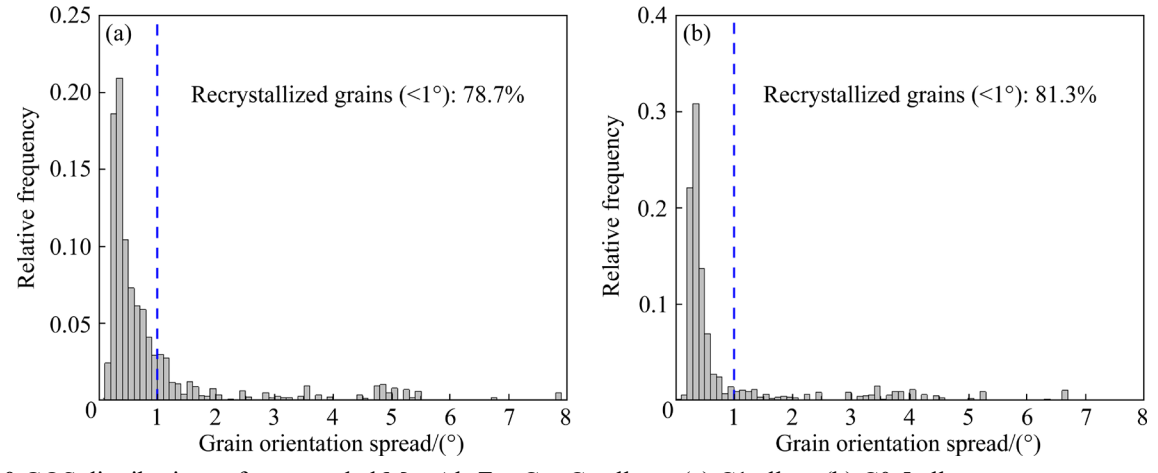


Fig. 10 GOS distributions of as-extruded Mg-Al-Zn-Cu-Ce alloys: (a) C1 alloy; (b) C0.5 alloy

Table 6 Correspondence between slip systems and Taylor axis in Mg alloys [23]

Taylor axis in Mg anoys [25]						
Deformation mode	Total number of slip variants	Taylor axis	Total number of variants of Taylor axis			
$(0001)\langle 11\overline{2}0\rangle$	3	$\langle 0\overline{1}10\rangle$	3			
$(10\overline{1}0)\langle 11\overline{2}0\rangle$	3	⟨0001⟩	1			
$(10\overline{1}1)\langle 11\overline{2}0\rangle$	6	$\langle 0\overline{1}12\rangle$	6			
$(10\overline{1}1)\langle\overline{1}\overline{1}23\rangle$	12	$\langle 1 3 \overline{8} \overline{5} 3\rangle$	12			
$(11\overline{2}2)\langle\overline{1}\overline{1}23\rangle$	6	$\langle 1\overline{1}00\rangle$	3			

Figure 11 presents kernel average misorientation (KAM) maps and the in-grain misorientation axe (IGMA) analysis results at the fracture of the as-extruded C1 and C0.5 alloys. The blue areas represent non-stress concentrated areas, while the green areas indicate stress concentrated areas. The IGMA distribution of Grains A-E is concentrated on the arc, which means the activation of the slip system of the basal plane $\langle a \rangle$ or pyramidal II $\langle c+a \rangle$. Owing to the lower critical resolved shear stress (CRSS), this $\langle uvt0 \rangle$ -type Taylor axis distribution is more likely to correspond to basal $\langle a \rangle$ slip. Furthermore, the activation of the prismatic $\langle a \rangle$ slip and pyramidal I $\langle a \rangle$ slip can also be found. For the C0.5 alloy, the activation slip systems include basal plane $\langle a \rangle$ slip, prismatic $\langle a \rangle$ slip, pyramidal I $\langle a \rangle$ slip, and pyramidal I $\langle c+a \rangle$ slip. Additionally, the deformation of C0.5 alloy is dominated by basal plane $\langle a \rangle$ slip and prismatic $\langle a \rangle$ slip. More activation of slip systems means better plasticity of alloy, which is why the plasticity of C0.5 alloy is better than that of C1 alloy. Moreover, extensive research has demonstrated that the solid solution of Zn and Cu atoms decreases the c/a axis ratio of α -Mg, leading to an increase in the CRSS of basal slip. This change also reduces the ratio of non-basal slip to basal slip CRSS, significantly enhancing the activity of non-basal slip.

5 Conclusions

- (1) The main SPs in the Mg-Al-Zn-Cu-Ce alloys are micron scale Al₃CuCe, micron scale MgZnCu, and nanoscale MgZnCu phases, and the particle size of SPs in C0.5 alloy is much finer than that in C1 alloy. The ultimate tensile strength, yield strength, and fracture strains of the C0.5 alloy reach 346 MPa, 312 MPa, and 11.7%, respectively.
- (2) The values of the Orowan strengthening and thermal expansion mismatch strengthening of the C0.5 alloy are 28 and 70 MPa, respectively, which are much higher than the values (15 and 47 MPa) of the C1 alloy.

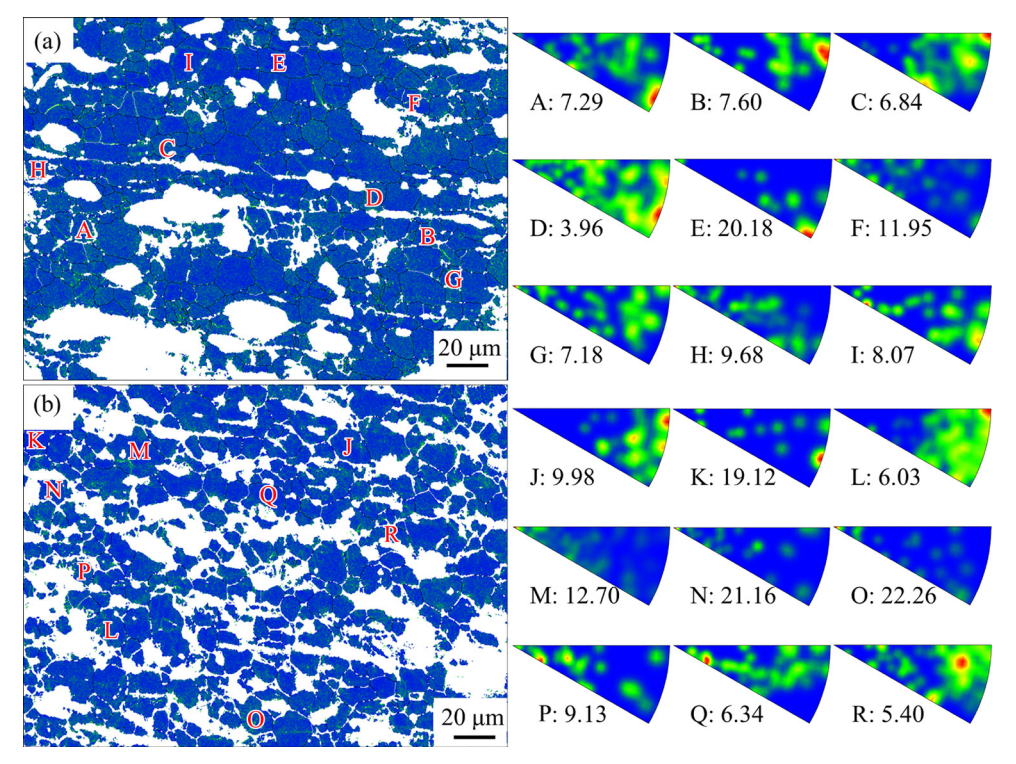


Fig. 11 KAM maps and IGMA analysis results at fracture of extruded Mg-Al-Zn-Cu-Ce alloys: (a) C1 alloy; (b) C0.5 alloy

- (3) Compared to the C1 alloy, the C0.5 alloy has a higher dynamic recrystallization rate and a lower maximum texture intensity, resulting in finer and more uniform grains. The slip systems of basal $\langle a \rangle$ slip, prismatic $\langle a \rangle$ slip, and pyramidal I $\langle a \rangle$ slip are initiated during the fracture of C1 alloy, and the basal $\langle a \rangle$ slip dominates the deformation of C1 alloy. The deformation of C0.5 alloy is dominated by basal plane $\langle a \rangle$ slip and prismatic $\langle a \rangle$ slip. This is the reason why C0.5 alloy has higher plasticity than C1 alloy.
- (4) The Young moduli of the MgZnCu, Al₃CuCe, and α -Mg phases are 121.6, 81.0, and 39.7 GPa, respectively. The Young moduli of the C1 and C0.5 alloys reach 58.5 and 60.0 GPa, respectively, because of the presence of MgZnCu and Al₃CuCe phases with high Young modulus.

CRediT authorship contribution statement

Zuo-hong GU: Investigation, Methodology, Data curation, Writing — Original draft, Writing — Review & editing; Yun-xuan ZHOU: Supervision, Methodology, Writing — Review & editing; Jia-xing PENG: Writing — Review & editing; Guang-ming HE: Validation, Formal analysis, Visualization; Hao LV: Investigation, Data curation; Quan DONG: Formal analysis, Visualization, Software; Jun TAN: Supervision, Funding acquisition, Methodology, Writing — Review & editing; Xian-hua CHEN: Methodology, Writing — Review & editing; Fu-sheng PAN: Supervision, Funding acquisition, Methodology, Writing — Review & editing; Jürgen ECKERT: Methodology, Writing — Review & editing.

Declaration of competing interest

The authors declare that they have no known competing financial interests or personal relationships that could have appeared to influence the work reported in this paper.

Acknowledgments

This work was financially supported by the National Key Research and Development Program of China (No. 2022YFB3709300), the Guangdong Major Project of Basic and Applied Basic Research, China (No. 2020B0301030006) and the Chongqing Special Project of Science and Technology Innovation, China (No. cstc2021yszx-jcyjX0007). The authors thank the Joint Lab for Electron Microscopy of Chongqing University and Analytical and Testing Center of Chongqing University (China).

References

- [1] ZHANG Y, FENG X H, HUANG Q Y, LI Y J, YANG Y S. Enhancing mechanical properties and degradation performance of Mg-0.8wt.%Ca alloy by directional solidification [J]. Transactions of Nonferrous Metals Society of China, 2023, 33(2): 409-421.
- [2] SUN Y H, ZHANG F, YANG B, REN J, SONG G S. Effect of extrusion ratio on microstructure, texture, and mechanical properties of dual-phase Mg-8Li-6Zn-2Gd alloy [J]. Transactions of Nonferrous Metals Society of China, 2024, 34(3): 833-845.
- [3] GUAN K, ZHANG J H, YANG Q, LI B S, WU R Z, MENG J. Effects of trace Ca addition on microstructure and mechanical properties of as-cast Mg-Sm-Gd-based alloy [J]. Transactions of Nonferrous Metals Society of China, 2023, 33(1): 46-58.
- [4] HUANG Y C, ZHANG Q D, OUYANG S J, SUN F Z, SUN J W, LI H Y, WU G H, CHEN P J, LIU W C. Effects of Zn and Gd contents and their ratios on microstructure and mechanical properties of as-cast and as-extruded Mg-8Li alloys [J]. Transactions of Nonferrous Metals Society of China, 2024, 34(3): 798-811.
- [5] DONG X, FENG L, WANG S, JI G, ADDAD A, YANG H, NYBERG E A, JI S. On the exceptional creep resistance in a die-cast Gd-containing Mg alloy with Al addition [J]. Acta Materialia, 2022, 232: 117957.
- [6] HUA Z M, WANG C, WANG T S, DU C F, JIN S B, SHA G, GAO Y P, JIA H L, ZHA M, WANG H Y. Large hardening response mediated by room-temperature dynamic solute clustering behavior in a dilute Mg-Zn-Ca-Sn-Mn alloy [J]. Acta Materialia, 2022, 240: 118308.
- [7] JIN Z Z, ZHA M, WANG S Q, WANG S C, WANG C, JIA H L, WANG H Y. Alloying design and microstructural control strategies towards developing Mg alloys with enhanced ductility [J]. Journal of Magnesium and Alloys, 2022, 10(5): 1191–1206.
- [8] WANG J, YUAN Y, CHEN T, WU L, CHEN X, JIANG B, WANG J, PAN F. Multi-solute solid solution behavior and its effect on the properties of magnesium alloys [J]. Journal of Magnesium and Alloys, 2022, 10(7): 1786–1820.
- [9] FAJARDO S, MIGUÉLEZ L, ARENAS M A, DE DAMBORENEA J, LLORENTE I, FELIU S. Corrosion resistance of pulsed laser modified AZ31 Mg alloy surfaces [J]. Journal of Magnesium and Alloys, 2022, 10(3): 756–768.
- [10] XU Y, HUANG Y, WANG Y, GAN W, WANG S, MAAWAD E, SCHELL N, HORT N. Investigations on the tensile deformation of pure Mg and Mg-15Gd alloy by in-situ X-ray synchrotron radiation and visco-plastic self-consistent modeling [J]. Journal of Magnesium and Alloys, 2023, 11(2): 607-613.
- [11] LV H, TAN J, YUAN Q, WANG F, ZHOU Y, DONG Q, TANG A, ECKERT J, JIANG B, PAN F. Recent advancements in thermal conductivity of magnesium alloys [J]. Journal of Magnesium and Alloys, 2024, 12(5): 1687–1708.
- [12] GU Z, ZHOU Y, DONG Q, HE G, CUI J, TAN J, CHEN X,

- JIANG B, PAN F, ECKERT J. Designing lightweight multicomponent magnesium alloys with exceptional strength and high stiffness [J]. Materials Science and Engineering A, 2022, 855: 143901.
- [13] WILLIAMS J J, PIOTROWSKI G, SAHA R, CHAWLA N. Effect of overaging and particle size on tensile deformation and fracture of particle-reinforced aluminum matrix composites [J]. Metallurgical and Materials Transactions A, 2002, 33(12): 3861–3869.
- [14] VETRANO J S, BRUEMMER S M, PAWLOWSKI L M, ROBERTSON I M. Influence of the particle size on recrystallization and grain growth in Al-Mg-X alloys [J]. Materials Science and Engineering A, 1997, 238: 101-107.
- [15] HE Y Y, BAI S W, FANG G. Coupled CA-FE simulation for dynamic recrystallization of magnesium alloy during hot extrusion [J]. Journal of Magnesium and Alloys, 2022, 10(3): 769–785.
- [16] WU Y, ZONG Y, JIN J. Grain growth in a nanostructured AZ31 Mg alloy containing second phase particles studied by phase field simulations [J]. Science China Materials, 2016, 59(5): 355–362.
- [17] ROSALIE J M, SOMEKAWA H, SINGH A, MUKAI T. Effect of precipitation on strength and ductility in a Mg-Zn-Y alloy [J]. Journal of Alloys and Compounds, 2013, 550: 114-123.
- [18] LI D, LAVENDER C. Strengthening and improving yield asymmetry of magnesium alloys by second phase particle refinement under the guidance of integrated computational materials engineering [J]. Journal of Engineering Materials and Technology, 2015, 137(3): 031008.
- [19] NAGASE T, TERAYAMA A, NAGAOKA T, FUYAMA N, SAKAMOTO T. Alloy design and fabrication of ingots of Al-Mg-Li-Ca light-weight medium entropy alloys [J]. Materials Transactions, 2020, 61(7): 1369–1380.
- [20] HUANG Y C, WEN J C, LIU Y, ZHAO Y X. Effects of electromagnetic frequency on the microstructure and mechanical properties of Al70Zn10Mg10Cu5Si5 medium entropy alloy [J]. Journal of Materials Research and Technology, 2022, 17: 3105–3117.
- [21] HAMMOND V H, ATWATER M A, DARLING K A, NGUYEN H Q, KECSKES L J. Equal-channel angular extrusion of a low-density high-entropy alloy produced by high-energy cryogenic mechanical alloying [J]. JOM, 2014, 66(10): 2021–2029.
- [22] TU T, CHEN X, ZHAO C, YUAN Y, PAN F. A simultaneous increase of elastic modulus and ductility by Al and Li additions in Mg–Gd–Zn–Zr–Ag alloy [J]. Materials Science and Engineering A, 2020, 771: 138576.
- [23] CHUN Y B, DAVIES C H J. Texture effect on microyielding of wrought magnesium alloy AZ31 [J]. Materials Science and Engineering A, 2011, 528: 3489–3495.
- [24] YE J, LI J, LUO H, TAN J, CHEN X, FENG B, ZHENG K, PAN F. Effect of micron-Ti particles on microstructure and mechanical properties of Mg-3Al-1Zn based composites [J]. Materials Science and Engineering A, 2022, 833: 142526.
- [25] LIN X Z, CHEN D L. Strain controlled cyclic deformation behavior of an extruded magnesium alloy [J]. Materials Science and Engineering A, 2008, 496: 106–113.

- [26] TU T, CHEN X, CHEN T, YUAN Y, PAN F. New high-modulus and high-strength Mg-Gd-Ag-Mn-Ge alloys [J]. Materials Science and Engineering A, 2021, 805: 140559.
- [27] XU Y, WANG S, WANG Y, CHEN L, YANG L, XIAO L, YANG L, HORT N. Mechanical behaviors of extruded Mg alloys with high Gd and Nd content [J]. Progress in Natural Science: Materials International, 2021, 31(4): 591–598.
- [28] ZHANG X, HU J, YE L, DENG Y, TANG C, YANG L, LIU Z. Effects of Si addition on microstructure and mechanical properties of Mg-8Gd-4Y-Nd-Zr alloy [J]. Materials & Design, 2013, 43: 74-79.
- [29] DING Z, ZHI X, LIU B, HOU H, ZHANG S, GUO W, CHEN D, ZHAO Y. Enhancement of strength and elastic modulus of Mg-Gd-Y-Zn-Zr alloy by Sn addition [J]. Materials Science and Engineering A, 2022, 854: 143885.
- [30] HU J, ZHANG X, TANG C, DENG Y, LIU Z, YANG L. Microstructures and mechanical properties of the Mg-8Gd-4Y-Nd-Zn-3Si (wt.%) alloy [J]. Materials Science and Engineering A, 2013, 571: 19-24.
- [31] FENG Z, ZHANG Y, TAN J, CHEN Y, CHEN Y, LI J, CHEN X, ZHENG K, PAN F. Large strain hardening of magnesium containing in situ nanoparticles [J]. Nanotechnol Rev, 2021, 10(1): 1018–1030.
- [32] CHENG J, GUO T, BARNETT M R. Influence of temperature on twinning dominated pop-ins during nanoindentation of a magnesium single crystal [J]. Journal of Magnesium and Alloys, 2022, 10(1): 169–179.
- [33] XIE Y, MENG X, ZANG R, CHANG Y, WAN L, HUANG Y. Deformation-driven modification towards strength-ductility enhancement in Al–Li–Mg–Zn–Cu lightweight high-entropy alloys [J]. Materials Science and Engineering A, 2022, 830: 142332
- [34] TAHREEN N, ZHANG D F, PAN F S, JIANG X Q, LI D Y, CHEN D L. Strengthening mechanisms in magnesium alloys containing ternary I, W and LPSO phases [J]. Journal of Materials Science & Technology, 2018, 34: 1110–1118.
- [35] YUAN W, PANIGRAHI S K, SU J Q, MISHRA R S. Influence of grain size and texture on Hall-Petch relationship for a magnesium alloy [J]. Scripta Materialia, 2011, 65: 994-997.
- [36] GUAN B, XIN Y, HUANG X, WU P, LIU Q. Quantitative prediction of texture effect on Hall-Petch slope for magnesium alloys [J]. Acta Materialia, 2019, 173: 142–152.
- [37] YU H, XIN Y, WANG M, LIU Q. Hall-Petch relationship in Mg alloys: A review [J]. Journal of Materials Science & Technology, 2018, 34: 248-256.
- [38] ZHANG Z, CHEN D L. Consideration of Orowan strengthening effect in particulate-reinforced metal matrix nanocomposites: A model for predicting their yield strength [J]. Scripta Materialia, 2006, 54: 1321–1326.
- [39] GOH C S, GUPTA M, WEI J, LEE L C. Characterization of high performance Mg/MgO nanocomposites [J]. Journal of Composite Materials, 2007, 41(19): 2325–2335.
- [40] MALLMANN C, HANNARD F, FERRIÉ E, SIMAR A, DAUDIN R, LHUISSIER P, PACUREANU A, FIVEL M. Unveiling the impact of the effective particles distribution on strengthening mechanisms: A multiscale characterization of Mg+Y₂O₃ nanocomposites [J]. Materials Science and

- Engineering A, 2019, 764: 138170.
- [41] DUNAND D C, MORTENSEN A. On plastic relaxation of thermal stresses in reinforced metals [J]. Acta Metallurgica et Materialia, 1991, 32(2): 127–139.
- [42] ARSENAULT R J, SHI N. Dislocation generation due to differences between the coefficients of thermal expansion [J]. Materials Science and Engineering, 1986, 81: 175–187.
- [43] KRESSE G, FURTHMüLLER J. Efficient iterative schemes for ab initio total-energy calculations using a plane-wave basis set [J]. Physical Review B, 1996, 54(16): 11169–86.
- [44] TOGO A, TANAKA I. First principles phonon calculations in materials science [J]. Scripta Materialia, 2015, 108: 1–5.
- [45] CUI J, YANG H, ZHOU Y, TAN J, CHEN X, SONG J, HUANG G, ZHENG K, JIN Y, JIANG B, PAN F. Optimizing the microstructures and enhancing the mechanical properties of AZ81 alloy by adding TC4 particles [J]. Materials Science and Engineering A, 2023, 863: 144518.
- [46] KIM C S, SOHN I, NEZAFATI M, FERGUSON J B, SCHULTZ B F, BAJESTANI GOHARI Z, ROHATGI P K, CHO K. Prediction models for the yield strength of

- particle-reinforced unimodal pure magnesium (Mg) metal matrix nanocomposites (MMNCs) [J]. Journal of Materials Science, 2013, 48(12): 4191–4204.
- [47] DAI L H, LING Z, BAI Y L. Size-dependent inelastic behavior of particle-reinforced metal-matrix composites [J]. Composites Science and Technology, 2001, 61(8): 1057–1063.
- [48] MEDINA J, GARCES G, PéREZ P, STARK A, SCHELL N, ADEVA P. High temperature mechanical behaviour of Mg-6Zn-1Y alloy with 1 wt.% calcium addition: Reinforcing effect due to I-(Mg₃Zn₆Y₁) and Mg₆Zn₃Ca₂ phases [J]. Journal of Magnesium and Alloys, 2020, 8(4): 1047-1060.
- [49] REN R, FAN J, WANG B, ZHANG Q, LI W, DONG H. Hall-Petch relationship and deformation mechanism of pure Mg at room temperature [J]. Journal of Alloys and Compounds, 2022, 920: 165924.
- [50] GUO F, ZHANG D, WU H, JIANG L, PAN F. The role of Al content on deformation behavior and related texture evolution during hot rolling of Mg-Al-Zn alloys [J]. Journal of Alloys and Compounds, 2017, 695: 396-403

协同提升轻质多组元 Mg-Al-Zn-Cu-Ce 合金的强度、塑性和刚度

古佐鸿¹,周云轩^{1,2,3},彭家兴¹,何光明¹,吕 颢¹,董 权¹, 谭 军^{1,2,3},陈先华^{1,2,3},蒋 斌^{1,3},潘复生^{1,2,3},Jürgen ECKERT^{4,5}

- 1. 重庆大学 材料科学与工程学院 国家镁合金材料工程技术研究中心, 重庆 400044; 2. 兰溪市镁材料研究院, 兰溪 321100;
 - 3. 重庆大学 高端装备铸造技术全国重点实验室, 重庆 400044;
 - 4. Erich Schmid Institute of Materials Science, Austrian Academy of Sciences,

Jahnstraße 12, A-8700, Leoben, Austria;

- 5. Department of Materials Physics, Montanuniversität Leoben, Jahnstraße 12, A-8700, Leoben, Austria
- **摘 要**:为了获得具有高抗拉强度、塑性和刚度的轻质多组元镁合金,设计了两种挤压态 $Mg_{92-5x}Al_{1.5+3x}Zn_{3-Cu_{3.5+x}Ce_x}(x=0.5$ 和 1,标记为 Co.5 和 Co.5 和

关键词: Mg-Al-Zn-Cu-Ce 合金; Al₃CuCe 相; 强化机制; 塑性变形机制; 力学性能

(Edited by Bing YANG)